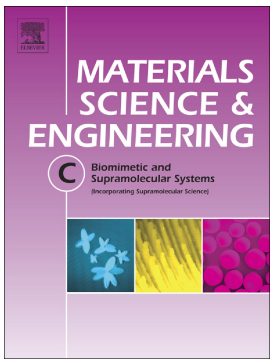

Effects of composition and hierarchical structures of calcium phosphate coating on the corrosion resistance and osteoblast compatibility of Mg alloys

Mingyu You, Mónica Echeverry-Rendón, Lei Zhang, Jialin Niu, Jian Zhang, Jia Pei, Guangyin Yuan

PII: S0928-4931(20)33653-5

DOI: https://doi.org/10.1016/j.msec.2020.111734

Reference: MSC 111734

To appear in: *Materials Science & Engineering C*

Received date: 28 August 2020

Revised date: 20 October 2020

Accepted date: 11 November 2020

Please cite this article as: M. You, M. Echeverry-Rendón, L. Zhang, et al., Effects of composition and hierarchical structures of calcium phosphate coating on the corrosion resistance and osteoblast compatibility of Mg alloys, *Materials Science & Engineering C* (2020), https://doi.org/10.1016/j.msec.2020.111734

Effects of composition and hierarchical structures of calcium phosphate coating on the corrosion resistance and osteoblast compatibility of Mg alloys

Mingyu You [a], Mónica Echeverry-Rendón [a], Lei Zhang [a], Jialin Niu [a], Jian Zhang [a, b], Jia Pei [a, *], and Guangyin Yuan [a, *]

[a] National Engineering Research Center of Light Alloy Net Forming & State Key Laboratory of Metal Matrix Composite, Shanghai Jiao Tong University, Shanghai, 200240, China

[b] Shanghai Innovation Medical Technology Co., Ltd. Shanghai 201306, China

Corresponding Author

* E-mail: jpei@sjtu.edu.cn; Tel.: +86 021-34203051.

* E-mail: gyyuan@sjtu.edu.cn; Tel.: +86-021-34203051.

Abstract

Magnesium and its alloys have been recently used in biomedical applications such as orthopedic implants, whereas the weak corrosion resistance undermines their clinical efficacy. Herein, to address this critical challenge, the preparation of hierarchically structured hydroxyapatite-based coatings was proposed. Compact coatings were fabricated on a Mg alloy through a facile two-step method of chemical deposition of brushite precursor and subsequent hydrothermal conversion. A series of HA-based coatings were obtained with kinetic conversion process with formation mechanism revealed. The hydroxyapatite coating demonstrated the greatest corrosion resistance for Mg in electrochemical and long-term immersion tests, especially against pitting corrosion, attributable to its compact structure, alkaline degradation environment and self-induced growth capacity. The *in vitro* cytocompatibility and osteoinductivity were dictated. Additionally, anti-corrosion mechanisms were compared among different coating compositions and structures, along with their correlation with cellular response. Our study brings hints for a tailored surface design for resorbable biomedical device applications.

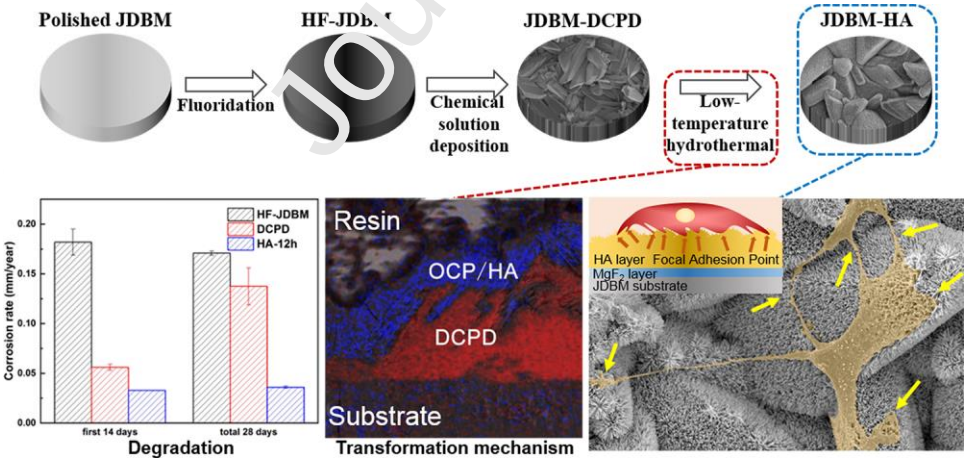

Keywords

Biodegradable magnesium alloy implant; hydrothermal conversion; corrosion resistance; calcium phosphate coatings; osteoblast compatibility

1. Introduction

Recently, Magnesium (Mg) and its alloys are considered as a promising candidate for next-generation bioresorbable implants for extensive biomedical applications, in particular, in the cardiovascular, orthopedic and dental implants fields [1]. For orthopedic implants, Mg has distinct advantages of biosafety, biodegradability, and matching mechanical properties; for instance, Young's modulus, which is lower compared to conventional biometals but similar as natural bones to obviate the risk of "stress shielding" [2]. During the degradation of Mg, release of magnesium ions (Mg^{2+}) and hydrogen gas (H_2) modify the physiological environment. Corrosion product as magnesium hydroxide ($Mg(OH)_2$) is dissolved by the action of chloride ions present in the body fluid to induce local alkalization, while the accumulation of H_2 produces subcutaneous gas pockets and necrosis of the surrounding tissue [3]. The dramatic changes at the interface, nevertheless, would inevitably affect the tissue healing and remodeling process, and ultimately the recovery of the patients. On the other side, the excessive corrosion nature of Mg may also lead to a rapid reduction of the mechanical integrity of the implant, causing a premature fracture. Hence, it has posed a pivotal challenge to simultaneously improve the corrosion resistance and biocompatibility of Mg for clinical applications. Alternative solutions predominantly fall into the categories of alloying and processing of Mg alloys, and surface modification of Mg-based substrates. Nonetheless, the incorporation of alloying elements in a Mg matrix modifies its mechanical properties, corrosion resistance, and biosafety in parallel [4].

On the other hand, surface modification presents as a more versatile approach to not only control the degradation rate but also to direct desirable biological response of implants. In this way, interactions between implants and tissues can be tailored by the properties of the developed coating.

Inspired on the composition of the bone, calcium phosphate (CaP) coatings such as brushite (DCPD), β-tricalcium phosphate (β-TCP), octacalcium phosphate (OCP), amorphous calcium phosphate (ACP) and hydroxyapatite (HA) have been used on Mg alloy implants, to facilitate osteointegration and inducing bioactivity . Specifically, HA is a major component of natural bones [5]. Synthetic HA is considered stable in the physiological environment with a lower degradation rate in comparison with the other CaP compounds mentioned above [6, 7]. HA can be used as coatings by physical deposition on the substrate or by growing *in-situ*, whereas one challenge lies in forming HA directly on Mg alloys, as the presence of Mg^{2+} ions inhibit HA crystallization in aqueous solutions [8]. Previous studies attempted to deposit HA on Mg alloys by using techniques like direct hydrothermal synthesis, sol-gel, and electro-deposition [9-12]. However, to date, crucial parameters of coating thickness, morphology, and most importantly, compactness are still under sub-optimal conditions. The development of HA coatings on Mg alloys with stable, controllable, and compact capabilities is thus imperative.

In comparison with other CaP coatings, DCPD is the most acidic and highly soluble (log K_{sp} = -6.59), which is more feasible to deposit on Mg alloys [6]. As a precursor of other CaPs, DCPD can progressively transform to HA *in situ* by hydrothermal reaction in an alkaline environment [13]. Previous researches focused on the transformation from unstable CaP coatings to HA coating on Ti substrate, while few study has been reported on Mg or Mg alloys so far [14-16]. Despite the efficiency in obtaining HA through this process, Su et al. reported problems of weak

corrosion resistance and high fragility of the obtained coating [17]. Therefore, it requires a systematic investigation of the reaction condition and formation mechanism from DCPD to HA on the substrates of Mg alloys, and in turn, the corresponding functionalities.

Apart from the composition of the coating, other surface properties, such as the morphology of a biomaterial, are also critical in modulating cell behavior. These features considerably regulate and determine the osseointegration, which is defined as a structural anchoring and functional connection between a load-carrying implant and ordered living bone without fibrous tissue formation at the interface [18]. Human bone consists of stratified structured micro- and nano-features with biofunctional behaviors [19]. Currently, a large number of studies were focusing on the design of surfaces, which simulate bone structure at the micro- and nano- level to improve cell behaviors, including cell adhesion, proliferation, differentiation, and mineralization [20, 21]. It is reasonable to speculate that the hierarchical design of the implants may exert a significant influence on bone tissue regeneration

In our previous study, a biodegradable DCPD coating was developed on a Mg-Nd-Zn-Zr (named JDBM) alloy [22] by chemical solution deposition, with a thickness of 10-30 μm [23]. Herein, due to the weak alkalinity and low degradation rate of HA, we hypothesized HA coating of optimized physicochemical properties could further suppress corrosion and increase biocompatibility of Mg. We developed a series of HA-based coatings through a hydrothermal treatment of DCPD precursor. In order not to impair the mechanical property of Mg substrates, the whole hydrothermal process was kept at a low temperature of 70 ℃. Morphology, composition and thickness of the coatings were optimized by controlling the hydrothermal reaction time at an optimal pH. The formation mechanism was analyzed during the coating

evolution process, where phase transitions were identified. The anti-corrosion behavior and mechanism was studied by immersion and electrochemical tests. Furthermore, *in vitro* biological evaluations were carried out with pre-osteoblasts to assess the effects of different CaP coatings on adhesion, proliferation, and osteogenic differentiation.

2. Materials and methods

2.1 Materials and sample preparation

Disc samples of Φ14 × 3 mm of biomedical JDBM alloy were used in the study. A precursor coating of DCPD was produced according to our previous work [23]. HA coatings were subsequently obtained by immersing the DCPD-coated samples in an alkaline solution, containing ethylenediaminetetraacetic acid calcium disodium salt hydrate ($(C_{10}H_{12}N_2O_8)CaNa_2$, Ca-EDTA, Sigma-Aldrich, USA), and sodium dihydrogen phosphate (NaH_2PO_4, Sinopharm Chemical Reagent Co., Ltd., China) at an optimized pH of 8.2. Afterwards, samples were subjected to low-temperature hydrothermal treatment at 70℃ in an autoclave, with varying time of 20 minutes (HA-20min), 1 hour (HA-1h), 3 hours (HA-3h), 6 hours (HA-6h) and 12 hours (HA-12h). Finally, samples were rinsed copiously with DI water and blown dried with streams of cold air. A schematic illustration of the coating preparation process is displayed in Fig. 1.

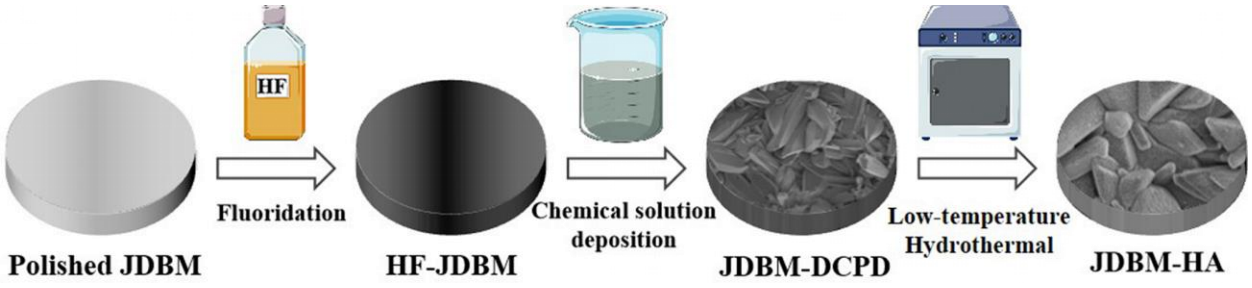

Figure 1. Schematic depiction of the fabrication process of the HA-based coatings on the Mg

alloy substrates.

2.2 Coating characterizations

The constituent phases of the coatings were identified by X-ray diffraction (XRD, D8 Advance, Germany). In order to analyze the coating microstructure and composition, samples were observed by scanning electron microscopy (SEM, MIRA3, Czech Republic and SEM, Siron 200, USA) coupled with energy-dispersive X-ray spectroscopy (EDS, Aztec X-MaxN80, Czech Republic and EDS, INCA X-Act, USA) following sputter-coated with a thin layer of gold (Quorum, Q150T Plus, England). For HA-20min samples, the cross-section was analyzed by Raman imaging combined with FE-SEM (RISE, MAIA3, Czech Republic).

2.3 *In vitro* corrosion/ degradation

2.3.1 Electrochemical tests

The electrochemical corrosion tests were carried out by immersion of the samples in Hanks' solution at 37 °C, recorded with an electrochemical work station (DH7000, Donghua, China). A sample with an exposed area of 1 cm^2 was considered as the working electrode, a saturated calomel electrode (SCE) as the reference, and graphite as the counter electrode. Open circuit potential curves were recorded by approximately 40 min to reach a steady state. Electrochemical impedance spectroscopy (EIS) measurements were performed within a frequency ranging from 100 kHz to 100 mHz. Potentiodynamic polarization curve was obtained with a scanning rate of 1 mV/s, and potential from −0.5 mV to 0.5 mV vs. open circuit potential. Impedance data was fitted and analyzed with ZSimpwin software (Version 3.50).

2.3.2 Immersion test

Samples with different coatings were immersed in alpha-modified Eagle's medium (α-MEM, Gibco, Invitrogen), supplemented with 1% penicillin and streptomycin (Gibco, Invitrogen) and incubated at 37 °C with 5% CO_2, and 95% humidity for up to 4 weeks. The Area/Volume (A/V) ratio of immersion was 1.25 cm^2/mL, following *in vitro* standards in ISO 10993-5. At an interval of 3-4 days during immersion, the concentrations of Mg^{2+}, Ca^{2+}, and P_i in the extracts were analyzed by an inductively coupled plasma atomic emission spectrometer (ICP-AES, iCAP6300, USA). pH values were measured by a pH meter (FE20, Mettler Toledo, Switzerland), and osmotic pressures with a freezing point osmometer (Osmolality 3000, Gonotec, Germany). The concentration of Mg^{2+} in the extracts was converted to the corrosion rates of the samples according to the following equation (eq. 1):

$$Mg + 2H_2O \longrightarrow Mg^{2+} + 2OH^- + H_2\,(g) \quad (1)$$

According to the standard ASTM G31-2012, the corrosion rate derived from the Mg^{2+} release was calculated by the equation (eq. 2):

$$\text{corrosion rate} = (K \times W) / (A \times T \times D) \quad (2)$$

Where the constant $K = 8.76 \times 10^4$, W is the mass loss (g), A the sample area (cm^2), T the time of exposure in hours (h), D the density (g/cm^3), and corrosion rate unit in mm/year.

At the 4 weeks of immersion, samples were removed from the medium, thoroughly rinsed and dried, coated with a thin layer of gold, and finally observed under SEM-EDS to examine the surface and cross-section.

2.4 *In vitro* cellular response

2.4.1 Preparation of sample extracts

Samples with different coatings were immersed in α-MEM under cell culture conditions for 3 days to obtain extracts according to ISO 10993-5. Subsequently, the extracts were filtered (0.22 μm, Millipore, US) and stored at 4℃.

2.4.2 Cell culture

Pre-osteoblast MC3T3-E1 (Cell Bank, Chinese Academy of Sciences) were cultured in α-MEM supplemented with 10% fetal bovine serum (FBS, Gibco, USA), 1% penicillin and streptomycin, and incubated at 37℃ with 5% CO_2 and 95% humidity. Fresh medium was replaced every two days. MC3T3-E1 cells from passages of 3-8 were used for the assays. Cells cultured in α-MEM with standard polystyrene culture plates (Corning, USA) were used as the control group.

2.4.3 Effects of extracts on cell viability

MC3T3-E1 cells were seeded in 96-well plates at a density of 5000 cells/cm^2 and incubated for 24 hours. Subsequently, the culture medium was replaced by 100 μL of sample extracts supplemented with 10% FBS. After 1, 3 days, respectively, the medium was replaced by 100 μL of fresh medium containing CCK-8 (CCK8, Beyotime Biotech, China) in a ratio of 10:1. Cells were incubated for 2 hours at 37℃, and optic density (OD) was measured by using a microplate reader (iMARK, Bio-Rad, USA) at a dual-wavelength of 450 nm and 655 nm.

2.4.4 Cell adhesion and proliferation assay & Microscopic Analyses

MC3T3-E1 cells were seeded directly on the samples of HF-JDBM, DCPD, HA-1h, HA-3h, and HA-12h, respectively, at a density of 5000 cells/cm^2 and cultured for 1 day and 3 days.

Afterwards, samples were gently rinsed twice with pre-warmed PBS, followed by cell fixation in 4% paraformaldehyde (PFA, Sigma-Aldrich, USA) for 30 minutes and permeabilization in 0.5% Triton X-100 for 5 minutes. After rinsing with PBS, cells were stained with Alexa Fluor 488 phalloidin (1:100 dilution in PBS, Invitrogen, USA) for 1 hour and DAPI (1:1000 dilution in PBS, Invitrogen, USA) for 20 minutes. Finally, samples were rinsed with PBS, and adherent cells were observed by fluorescence microscopy (IX71, Olympus, Japan). For the quantification of the cells, at least 8 photos were taken for each sample and analyzed using the software ImageJ (version 1.51K).

2.4.5 Observation of adherent cells using SEM

MC3T3-E1 cells were seeded on the samples with different coatings at a density of 20000 cells/cm^2 and allowed for attachment for 24 hours. Subsequently, samples were rinsed twice with PBS, and adherent cells were fixed with 4% PFA for 30 minutes, followed by exposure to gradient ethanol dehydration (30, 50, 70, 80, 90 and 100%). Finally, samples were carefully air-dried and coated with a thin film of gold for 45 seconds for observation in SEM.

2.4.6 Measurement of alkaline phosphatase (ALP) activity

MC3T3-E1 cells were seeded in 6-well plates at a density of 1000 cells/cm^2. After 24 hours, the medium was replaced with the differentiation medium, consisting of the sample extracts supplemented with 10% FBS, 0.1 μM dexamethasone, 50 μM ascorbic acid, and 10 mM β-glycerophosphate (all from Sigma, USA). Cells treated only with standard differentiation medium were used as the blank control, while cells growing with α-MEM supplemented with 10% of FBS as the negative control.

After 7 and 14 days of culture, cells were treated with 0.1% Triton-100 and were frozen and thawed twice to obtain the cell lysis. The total protein content was quantified by using a BCA Protein Assay Kit (Thermo Fisher Scientific, USA). ALP activity of MC3T3-E1 cells was measured by using p-nitrophenyl phosphate reagent (pNPP, Sigma, USA) according to the manufacturer's instructions. Absorbance was measured with a microplate reader at 415 nm, by which ALP activity was calculated and normalized to the total protein content.

2.5 Statistical analysis

All data were shown as mean ± standard deviation (SD) from triplicate independent experiments. The results were analyzed with Student's t-test or one-way analysis of variance (ANOVA) using SPSS software (Version 24, IBM, USA). p-value < 0.05 was considered statistically significant.

3. Results

3.1 Characterizations of calcium phosphate coatings

The formation process of as-synthesized CaP coatings was observed with SEM, as displayed in Fig. 2a. Initially, the grains of the precursor coating of DCPD appeared granite-shaped with a diameter of 50-100 μm. After 20 minutes of low-temperature hydrothermal treatment, the morphology of the sample (HA-20min) in nanoscale became roughened uniformly. Subsequently, the coating in nanoscale transformed into spheroidal-like nanocrystals (HA-1h), which then further grew into nanorods morphology (HA-3h). After 6 hours (HA-6h), the surface of the microscale grains was densely covered with nanoneedle-like crystals, while a similar feature of longer needles was observed after 12 hours (HA-12h). The topography of coatings in the micro-scale remained almost unchanged during the overall hydrothermal process. The thickness

of the initial DCPD coating was about 5-25 μm. While no significant change of thickness was observed after hydrothermal reaction for 20 minutes and 1 hour, the entire coating thicknesses increased gradually to 9-30 μm, 15-38 μm, and 20-40 μm after 3, 6 and 12 hours, respectively.

In Fig. 2b, EDS results confirmed that the Ca/P atomic ratio of the DCPD pre-coating was about 1.13 ± 0.12, similar to its stoichiometric ratio (1:1). After 12 h of hydrothermal treatment, the atomic ratio of the coating (HA-12h) significantly increased to 1.66 ± 0.13, which is close to the stoichiometric ratio of HA (Ca/P ratio = 1.67). Further information on the phase transformation during the entire hydrothermal process was demonstrated with XRD pattern analysis (Fig. 2c). Characteristic peaks of OCP (Joint Committee for Powder Diffraction Studies, JCPDS, 44-0778) at a 2θ = 4.8°, DCPD (JCPDS 09-0077) at a 2θ = 11.7° and HA (JCPDS 24-0033) at a 2θ = 32.9° were identified. Prior to the hydrothermal reaction, the XRD pattern of the DCPD sample was detected to confirm the composition. After 20 minutes, both characteristic peaks of OCP and HA were detected on the coating (HA-20min), whereas the intensity of DCPD was decreased. As for HA-1h, the DCPD signal completely disappeared, the intensity of OCP characteristic peaks remarkably increased, and the signal of HA emerged. Afterwards, the characteristic peak of OCP at a 2θ = 4.8° decreased gradually, while the intensity of HA peaks within the angular region from 31° < 2θ < 35° increased observably. After 12 hours, the coating was mainly composed of HA, indicating a complete phase transformation.

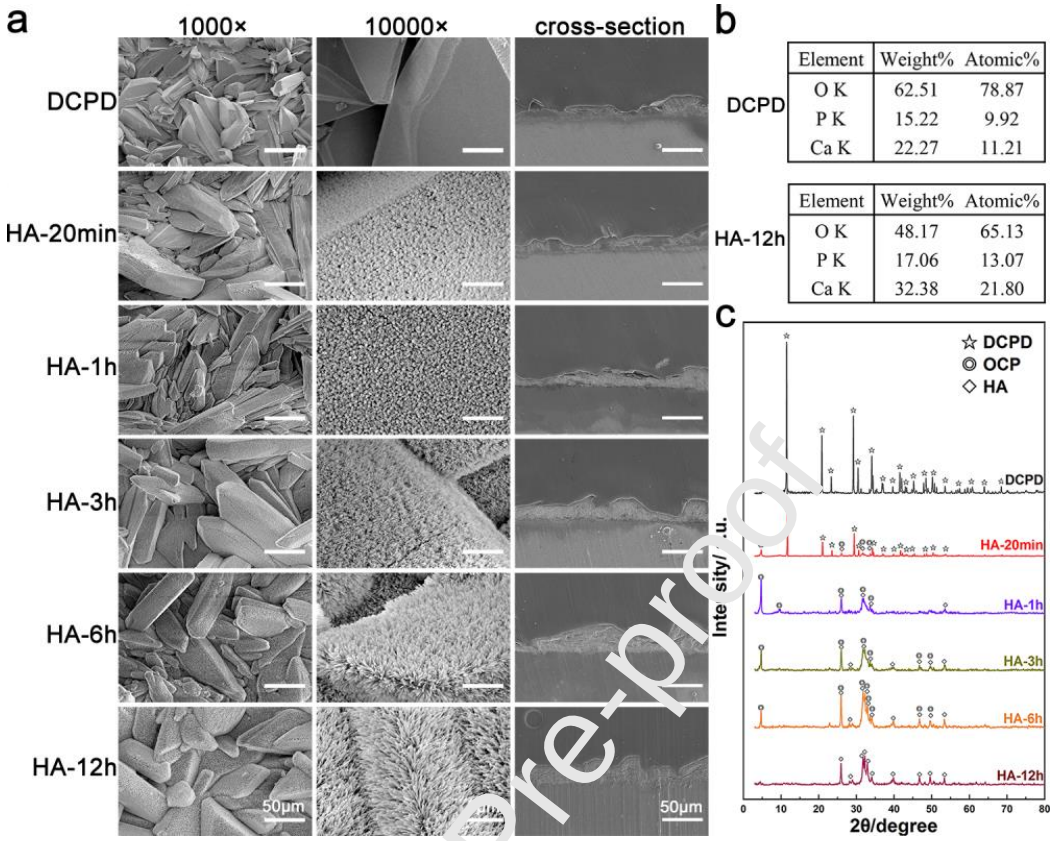

Figure 2. (a) SEM images of the top surface and cross-section, (b) EDS results, and (c) XRD spectra of DCPD, HA-20min, HA-1h, HA-3h, HA-6h, and HA-12h coatings.

In order to investigate the transformation mechanism from DCPD to OCP and HA during the initial hydrothermal process, Fig. 3a showed the analysis of the HA-20min cross-section through the examination of RISE (a combination of confocal Raman microscopy and SEM). This technique brings simultaneous and detailed information about the structural, elemental, and molecular composition of the coating [24]. In the Raman spectra, DCPD was labeled with red color, and OCP/HA with blue color (Fig. 3b), to reveal the relative distribution of DCPD and OCP/HA components in the coating. OCP/HA was obtained mainly in the outermost layer while DCPD predominately existed in the inner.

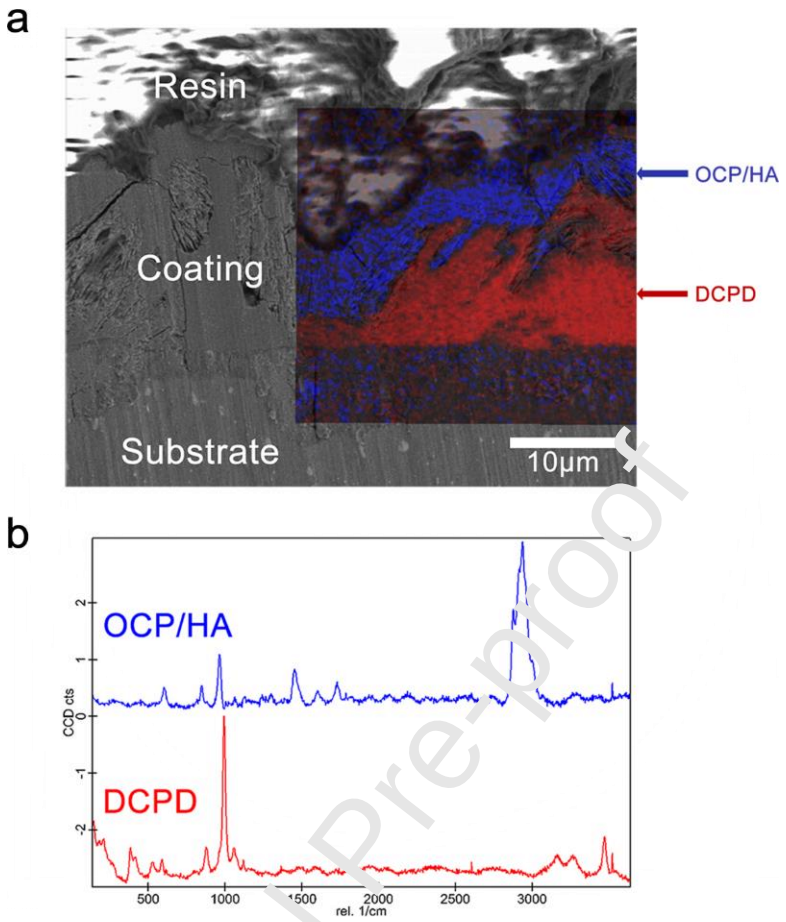

Figure 3. (a) RISE imaging and (b) Raman spectra of the cross-section area of the HA-20min coating.

In addition, the bonding strength between the HA-12h coating and the Mg substrate was measured with tensile test as about 2 MPa, indicating that the obtained HA coating adequate interfacial binding to meet the requirements for orthopedic applications.

3.2 *In vitro* corrosion/ degradation

Electrochemical evaluations such as potentiodynamic polarization and electrochemical impedance spectroscopy have been widely used to study corrosion mechanisms. Electrochemical corrosion results coated JDBM were shown in Fig. 4. It was observed from Fig. 4a that the open

circuit potential stabilized at -1.33V, -1.30V, and -1.17V for HF-JDBM, DCPD and HA-12h samples, respectively. The positive shift of potential implied a lower tendency of HA-12h towards corrosion from the perspective of thermodynamics. Fig. 4b displayed the potentiodynamic polarization curves of the three coating groups. The corrosion potential (E_{corr}) and the corrosion current densities (I_{corr}) were calculated by Tafel fitting, while the pitting corrosion potential (E_{pit}) was extrapolated from the polarization curves (Table 1). The I_{corr} of the HF-JDBM, DCPD, and HA-12h sample were 4.17 μA/cm^2, 3.45 μA/cm^2, and 2.06 μA/cm^2, respectively, indicating a most decelerated corrosion with the HA-12h coating. In the anodic polarization range, the slope of the HA-12h curve was much sharper than the others, signifying a most enhanced polarizability and decelerated corrosion with the HA-12h coating. Meanwhile, the E_{pit} of the HF-JDBM and DCPD sample were -1.14V and -1.01V, revealing that the DCPD coating slightly increased the pitting corrosion resistance of JDBM. Moreover, no pitting potential of HA-12h occurred in the scan range, indicating the pitting corrosion resistance of JDBM is greatly enhanced by coating compact hydroxyapatite.

For the characteristic impedance spectra, Nyquist plots consisting of single capacitive loops were shown in Fig. 4c, along with the corresponding equivalent circuits (EC) applied to fit the EIS results and displayed in Fig. 4d. For the coated-JDBM, the corrosion resistance was clearly enhanced when a larger diameter of high frequency capacitive loop appeared in the Nyquist plots. The EC of the single-layer HF-JDBM was different from those of DCPD and HA-12h samples with double layers. In this EC model, R_s was the solution resistance; C_f and R_f were capacity and resistance of DCPD or HA-12h coating; CPE_b and R_b represented the magnesium fluoride (MgF_2) layer as a barrier after JDBM fluorination. C_{dl} referred to the electric double layer capacity between the MgF_2 layer and substrate, and R_{ct} was the charge transfer resistance. Due to the

invasion of Cl^- to the MgF_2 layer, the solution could permeate through the coatings and interacted with the JDBM. The charge transfer process occurred and an electric double layer formed, described by a CPE_{dl} and a R_{ct} in parallel. The corrosion mechanisms were generally fitted well with the EC model, and the fitted parameters were summarized in Table 2. The R_{ct} value of HF-JDBM sample was calculated as of 836 $\Omega \cdot cm^2$, which was increased with the DCPD coating to 1089 $\Omega \cdot cm^2$, while the R_{ct} value of HA-12h reached 3197 $\Omega \cdot cm^2$, demonstrating the impeding effect with the DCPD coating and the excellent corrosion resistance of HA-12h coating on JDBM substrates.

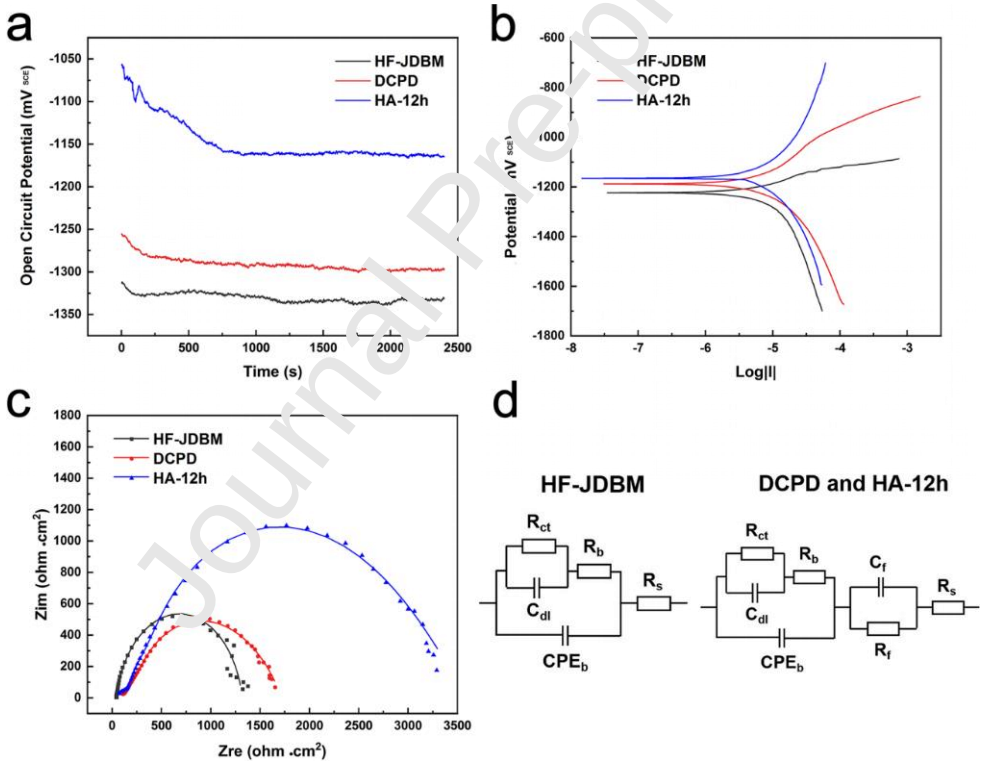

Figure 4. Electrochemical corrosion results of the HF-JDBM, DCPD and HA-12h samples in Hanks' solution: (a) open circuit potential curves, (b) potentiodynamic polarization curves, (c) Nyquist plots and (d) equivalent circuits used for fitting the EIS spectra.

	E_{corr} (V)	I_{corr} (μA/cm^2)	E_{pit} (V)
HF-JDBM	-1.22	4.17	-1.14
DCPD	-1.19	3.45	-1.01
HA-12h	-1.16	2.06	not found

Table 1. E_{corr}, I_{corr} and E_{pit} values of the HF-JDBM, DCPD and HA-12h samples obtained from the potentiodynamic polarization curves.

	R_s ($\Omega\cdot cm^2$)	C_f ($S\cdot cm^{-2}\cdot s^{-1}$)	R_f ($\Omega\cdot cm^2$)	CPE_b ($S\cdot cm^{-2}\cdot s^{-1}$)	n	R_b ($\Omega\cdot cm^2$)	C_{dl} ($S\cdot cm^{-2}\cdot s^{-1}$)	R_{ct} ($\Omega\cdot cm^2$)
HF-JDBM	41.3			2.66×10^{-5}	0.889	414	1.64×10^{-6}	836
DCPD	41.9	1.34×10^{-8}	64.9	3.21×10^{-5}	0.646	530	3.25×10^{-6}	1083
HA-12h	38.4	6.85×10^{-6}	175	3.25×10^{-5}	0.506	187	5.79×10^{-6}	3197

Table 2. Electrochemical parameters determined from fitting Nyquist plots of the HF-JDBM, DCPD and HA-12h samples.

The degradation profiles and characteristics were also evaluated by the actual immersion test in the cell culture medium. In Fig. 5a, it showed an improvement in corrosion resistance of the HA-12h sample in comparison with the HF-JDBM through the analysis of Mg^{2+} release curves. It was possible to observe within the enlarged view of the plot in the first 7 days that the Mg^{2+} release of the HA-12h further reduced 39.0% of that of DCPD. In the first 14 days post

immersion, as compared to the high corrosion rate of HF-JDBM of 0.182 mm/year, for DCPD it was of 0.056 mm/year and for HA-12h was of 0.033 mm/year, which corresponds to a marked decrease by 69.2% and 81.9%, respectively (Fig. 5b). The corrosion rate of the HF-JDBM sample remained consistent until day 28, which was 0.171 mm/year. Interestingly, the DCPD group revealed a drastic rise of corrosion rate from 14-28 days, which slightly exceeded that of the HF-JDBM, and the corrosion rate for total 28 days reached a lower level as compared to HF-JDBM with 0.137 mm/year. On the contrary, HA-12h sample showed a steady, and the slowest release profile with a calculated corrosion rate of 0.036 mm/year during the whole period, which represented a considerable enhancement of corrosion-resistance by 78.9% and 73.7% in 4 weeks compared to HF-JDBM and DCPD, respectively

Throughout the overall process, the pH value of the HA-12h extract kept at 7.59-7.81, which was the most similar to that of the physiological environment among the three samples. It was slightly higher than that of α-MEM (measured as 7.60), while the extract of HF-JDBM was the most alkaline with a pH of 7.77-8.07 (Fig. 5c). Intriguingly, the pH change of DCPD extract displayed a biphasic profile, which slightly increased to 7.74 in the first 3 days, followed by a gradual decrease to 7.40 until day 7, which afterwards elevated to 8.03 in the end. The osmolality values in the sample extracts generally followed a similar trend as that of the pH (Fig. 5d).

As shown in Fig. 5e and 5f, we also observed that the curves displayed different variation trends for different coating groups. The Ca^{2+} concentration of HF-JDBM appeared below that of α-MEM in the first 21 days, and then rose to the initial level of about 67.0 ppm. Intriguingly, in the DCPD extract, it first increased from 68.3 ppm to 91.0 ppm on day 1, which then gradually dropped to approximately 30.0-40.0 ppm, even lower than that of the α-MEM (68.3 ppm). As for HA-12h, following a decrease to roughly 34.4 ppm on the first day, it stabilized in the range of

33.0-42.3 ppm. Regarding the P_i concentration, it was evident that for DCPD it explosively grew to 122.9 ppm on day 10, and quickly declined to 18.5 ppm at the end of the experiment, while for HA-12h and HF-JDBM it revealed a gentle decrease from 29.2 ppm to 19.0 ppm.

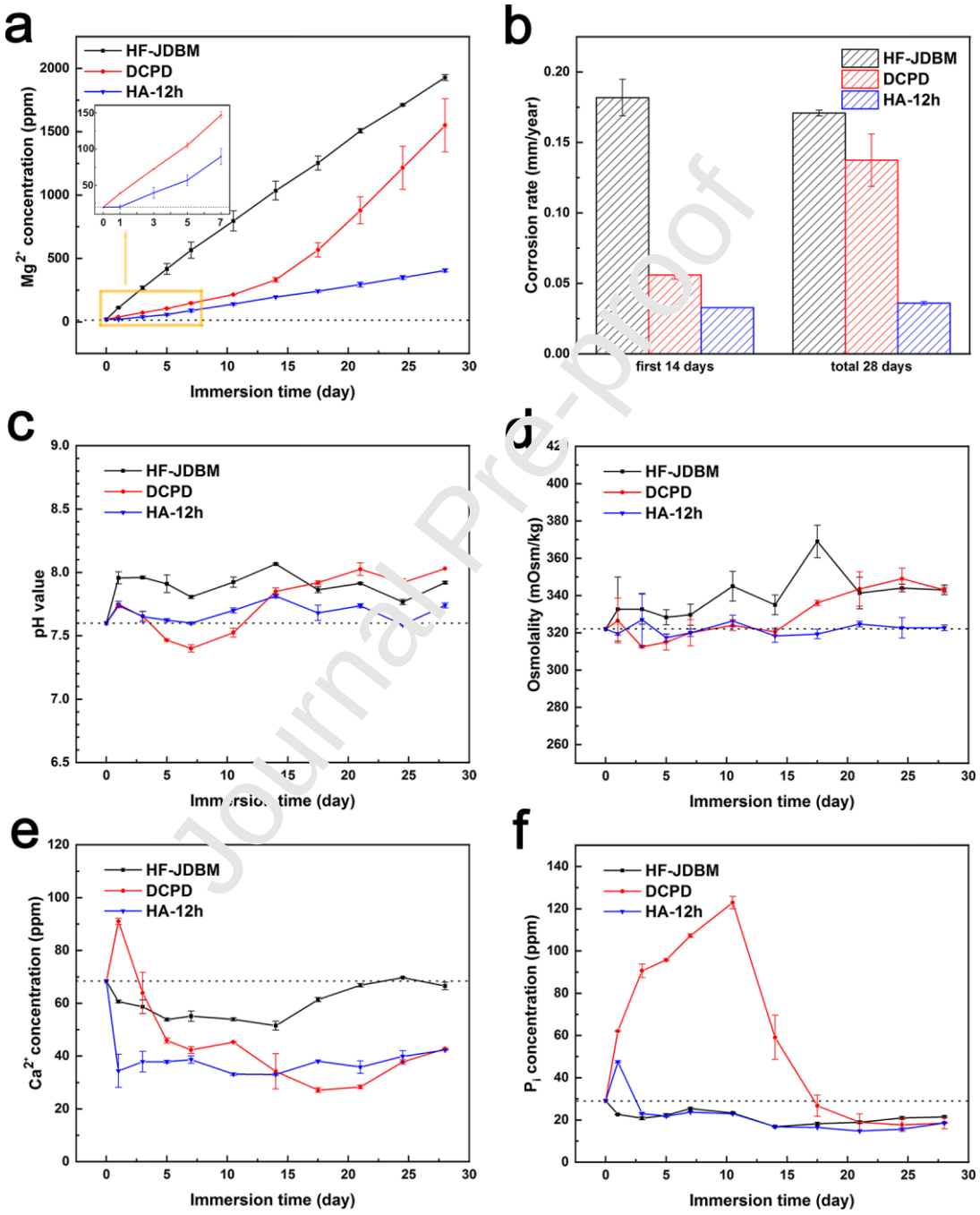

Figure 5. (a) Cumulative Mg^{2+} release, (b) calculated corrosion rate, (c) pH value, (d) osmolality,

(e) Ca^{2+} concentration, and (f) P_i concentration of the extracts of HF-JDBM, DCPD and HA-12h in α-MEM for 28 days immersion.

Results of SEM-EDS from the samples of HF-JDBM, DCPD, and HA-12h post the immersion test were shown in Fig. 6. As for the HA-12h sample, the morphology remained almost intact in micro-scale, and surface needle-like crystals transformed to coralloidal morphology in nanoscale, while the HF-JDBM presented a deeply cracked surface appearance, and the DCPD displayed fissures and flower-like crystals with some defects and cracks occasionally found. On the contrary, in the cross-section view, the thickness of the HA-12h coating increased to 32-85 μm, while no crack or defect was observed on the surface, implying the induction of *in-situ* growth of HA in the medium. The HF-JDBM showed a degradation product layer of 15-20 μm thick, and corrosion pits penetrating the substrate were observed in the DCPD. According to the EDS results, high intensities of Ca and P signals of the three samples were all detected, with signal of Mg substrate decreased. The ratios of Ca/P of HF-JDBM, DCPD, and HA-12h samples were 0.88 ± 0.06, 1.46 ± 0.10, and 1.62 ± 0.07, respectively, which were much closer to the stoichiometric Ca/P ratio of hydroxyapatite (1.67), indicating the self-induced growth capacity of HA in the culture medium.

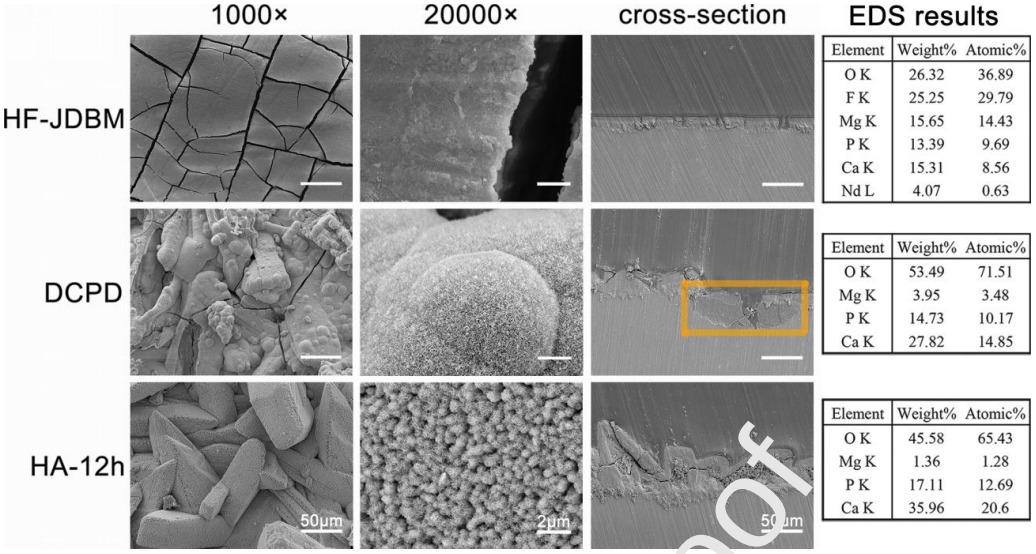

Element	Weight%	Atomic%
O K	26.32	36.89
F K	25.25	29.79
Mg K	15.65	14.43
P K	13.39	9.69
Ca K	15.31	8.56
Nd L	4.07	0.63

Element	Weight%	Atomic%
O K	53.49	71.51
Mg K	3.95	3.48
P K	14.73	10.17
Ca K	27.82	14.85

Element	Weight%	Atomic%
O K	45.58	65.43
Mg K	1.36	1.28
P K	17.11	12.69
Ca K	35.96	20.6

Figure 6. SEM surface and cross-section micrographs, and EDS results of HF-JDBM, DCPD and HA-12h samples after immersion under cell culture condition for 28 days.

3.3 Effects of extracts on cell viability

The viability of MC3T3-E1 cells incubated with sample extracts was tested with CCK-8 assay. In Fig. 7a, MC3T3-E1 cells cultured in the presence of the extracts of all the groups revealed remarkable cell growth after 3 days, as indicated by the increment of OD values. Cells exposed to the extract from DCPD and HA-1h showed a significantly higher cell proliferation in terms of mitochondrial activity in comparison with the control group. Cells treated with the extracts of HA-3h and HA-12h displayed nearly identical behavior to that of the control group with no statistical difference.

3.4 Cell adhesion and proliferation on coated-JDBM

Fig. 7d presented fluorescence staining images of nuclei of the attached cells, cultured for 1 day and 3 days on the samples. Statistical analysis of adherent cell density was illustrated in Fig. 7b.

On day 1, the HF-JDBM group had a noticeable inhibitory effect on cell adhesion as compared to the control group, while a general trend of improvement on cell adhesion was observed as for DCPD, HA-1h, HA-3h, and HA-12h samples, showing 192.8%, 149.0%, 137.3%, and 125.9% of the control group. On day 3, in contrast to a distinct increase in cell number in the control group, for the HF-JDBM, it exhibited rather poor proliferation profile, suggesting high cytotoxicity. While for DCPD, HA-1h, HA-3h and HA-12h groups, they showed slightly lower cell number than the control group. In Fig. 7e and 7f, cells in the control group showed typical and widespread morphology with clear dorsal stress fibers. Cells on the HF-JDBM exhibited similar morphologies to those on the control but appeared smaller, whereas the MC3T3-E1 cells on the DCPD and HA-1h samples showed an elongated shape with attachment to the edge of the grains. On the HA-3h and HA-12h groups, the cells became polygonal-shaped, with the presence of filopodia and well-formed cell-cell adhesions commonly indicating an optimal attachment and intercellular communication.

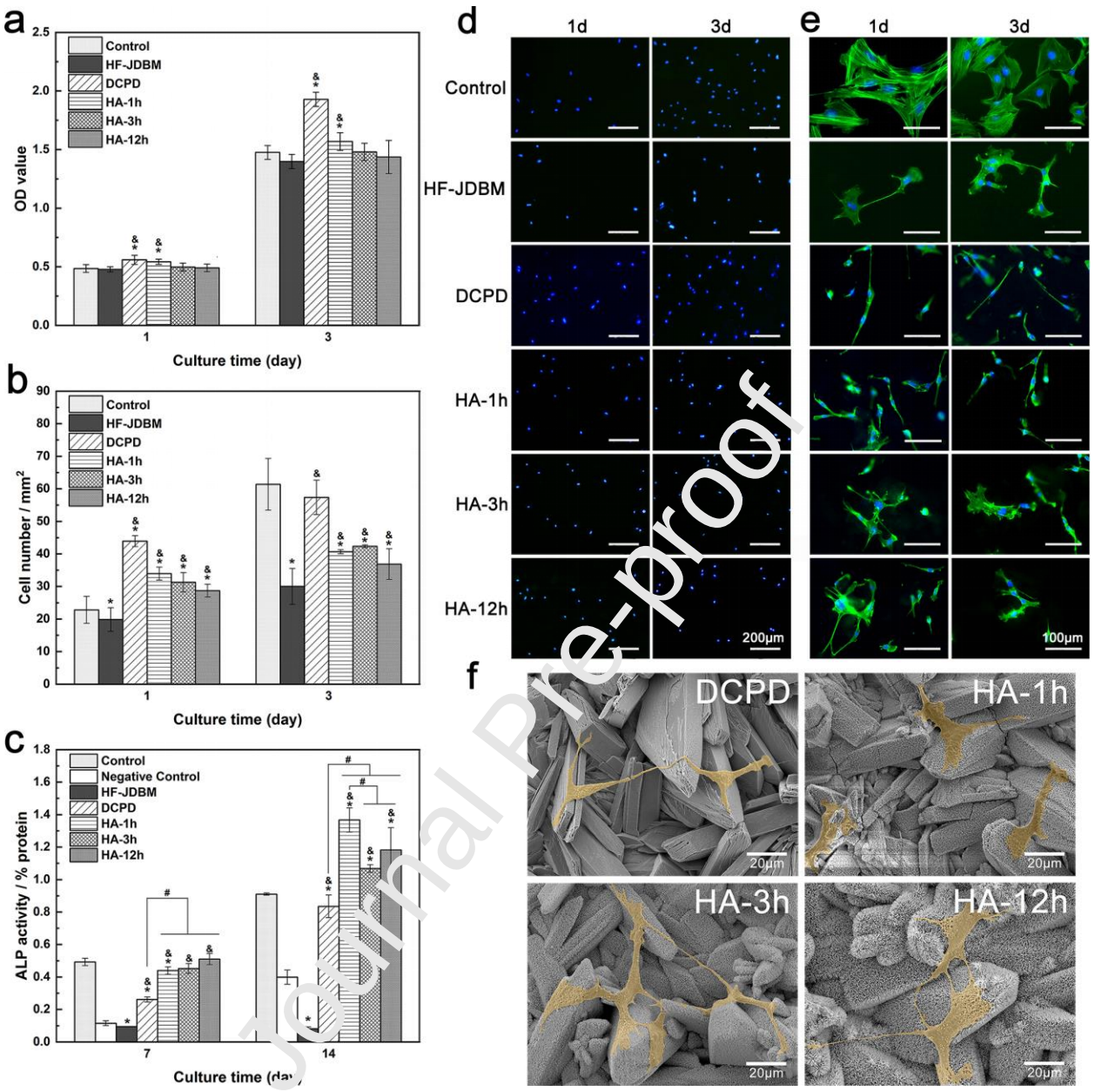

Figure 7. (a) CCK-8 assay results of MC3T3-E1 cells cultured in the sample extracts for 1 day and 3 days, (b) Statistical analysis of adherent MC3T3-E1 cells on the samples for 1 day and 3 days, (c) ALP activity of MC3T3-E1 cells for 7 day and 14 days, (d) fluorescence microscopy images of cell nucleus and (e) cytoskeleton staining on the samples after culturing for 1 day and 3 days of HF-JDBM, DCPD, HA-1h, HA-3h and HA-12h, and (f) the SEM images of adherent MC3T3-E1 cells on the samples after 1-day culture. *Blue*, nuclei stained with DAPI. *Green*, actin

cytoskeleton stained with phalloidin. # $p < 0.05$. * $p < 0.05$ between the test group and the control group. & $p < 0.05$ between the test group and the HF-JDBM group.

3.5 ALP activity measurement

ALP is a crucial marker to measure the potential ability of osteoblastic differentiation and osteogenesis at the early stage. In Fig. 7c, the ALP activities of MC3T3-E1 in control, HA-3h, and HA-12h were similar after 7 days of incubation. After 14 days, the ALP values of HA-1h, HA-3h, and HA-12h were appreciably higher than that of the control group by 50.5%, 17.6%, 29.7%, implying promoted osteogenic differentiation of MC3T3-E1 cells. Notably, cells cultured in the presence of the DCPD group appeared slightly lower ALP activity than the control, while cells in the HF-JDBM barely expressed ALP activity.

4. Discussion

4.1 Mechanism of the HA formation process

The heterogeneous nucleation of DCPD was initiated upon the degradation of the JDBM substrate, where local pH at the metal-solution interface increased, thus facilitating the deposition of DCPD [23]. Afterwards, microscale, coarse grains were observed on the DCPD sample. The interfacial reactions to achieve DCPD deposition are described in eq. 3 and eq. 4:

$$Ca^{2+} + H_2PO_4^- + 2H_2O \longrightarrow CaHPO_4{\cdot}2H_2O\ (s) + H^+ \qquad (3)$$

$$Mg + 2H^+ \longrightarrow Mg^{2+} + H_2\ (g) \qquad (4)$$

OCP, a more alkaline calcium phosphate phase in comparison with DCPD, can convert to HA by further hydrolyzing, signifying a transition phase between DCPD and HA [25]. According to

the XRD result (Fig. 2b), it was within one hour that DCPD fulfilled complete transformation to OCP and HA. The transformation from DCPD to OCP thus can be described by the following reaction (eq. 5):

$$6CaHPO_4 \cdot 2H_2O\ (s) + 2[(C_{10}H_{12}N_2O_8)Ca]^{2-} + 4OH^- \longrightarrow Ca_8(HPO_4)_2(PO_4)_4 \cdot 5H_2O\ (s) + 11H_2O + 2(C_{10}H_{12}N_2O_8)^{4-} \quad (5)$$

The mechanism of the initial conversion of DCPD coating was studied by the analysis of HA-20min. The cross-section of HA-20min was separated into two layers of coexistence of three phases, the outermost layer of OCP and HA and the inner of remaining DCPD. This observation implied an *in-situ* conversion mechanism of part of the DCPD coating to a mixture of OCP and HA. Furthermore, based on others' previous findings [14], it is thus most probably attributable to a continuous process of local dissolution and reprecipitation mechanism.

Afterwards, OCP transformed gradually into HA following the reaction:

$$Ca_8(HPO_4)_2(PO_4)_4 \cdot 5H_2O\ (s) + 2[(C_{10}H_{12}N_2O_8)Ca]^{2-} + 4OH^- \longrightarrow Ca_{10}(PO_4)_6(OH)_2\ (s) + 7H_2O + 2(C_{10}H_{12}N_2O_8)^{4-} \quad (6)$$

Thus the overall reaction can be presented as below：

$$6CaHPO_4 \cdot 2H_2O\ (s) + 4[(C_{10}H_{12}N_2O_8)Ca]^{2-} + 8OH^- \longrightarrow Ca_{10}(PO_4)_6(OH)_2\ (s) + 18H_2O + 4(C_{10}H_{12}N_2O_8)^{4-} \quad (7)$$

In addition, it was observed that the thicknesses of the samples were time-variable, which was presumable to have the deposition of HA on the top surface. The equation is thus described as follows:

$$10[(C_{10}H_{12}N_2O_8)Ca]^{2-} + 6PO_4^{3-} + 2OH^- \longrightarrow \quad Ca_{10}(PO_4)_6(OH)_2\,(s) + 10(C_{10}H_{12}N_2O_8)^{4-} \qquad (8)$$

In the beginning of the hydrothermal process, DCPD was converted to HA by a low-temperature (Fig. 1). During 12 hours, the micro-morphology remained similar, whereas notable changes at the nanoscale could be observed. While the coating morphology became roughened in nanoscale, and then it evolved to spheroidal-like and needle-like nanocrystals successively.

In this process, it can be inferred that the pH value on the coating surface increases because of the Mg degradation (eq. 1), supplying OH^- ions to accelerate the nucleation and growth of OCP and HA. Furthermore, as the calcium element is one of the indispensable reagent, and the P_i ions are buffer agents to form a uniform coating by maintaining pH stability, the treatment solution should reach a high concentration of both calcium and phosphate ions for HA crystallization in an alkaline environment. Ca-EDTA is a chelate of calcium with hypotoxicity and high solubility up to 1.2 M in aqueous solution at room temperature, which has higher K_{sp} than inorganic Ca salts. Additionally, Ca-EDTA provides a wide pH range for the synthesis of OCP and HA coatings, compared to other calcium chelate compounds such as calcium lactate and calcium gluconate [26]. In agreement with previous studies, it demonstrated that the HA crystals grew along the c-axis orientation proportionally with the increase of the reaction time in NaOH solution at an appropriate temperature 60-100 ℃, which could be controlled to decompose Ca-EDTA and to induce the reactions [27]. The [001]-oriented rod-like nanocrystals continually grew to nanoneedles due to the attraction of COO^- groups in EDTA and the calcium ions along the c-axis in HA [28].

4.2 Degradation characteristics and possible mechanism

In order to improve the durability and mechanical resistance of biodegradable orthopedic implants, a layer of MgF_2 was first produced by exposing JDBM to hydrofluoric acid [29]. MgF_2 layer acted as a barrier initially to slow down the corrosion rate; however, it can be dissolved gradually in Cl^- containing solution, causing defects in the coating and weakening the protective effects in the long-term test as described in eq. 9 [29, 30].

$$MgF_2\ (s) \xrightarrow{Cl^-} Mg^{2+} + 2F^- \qquad (9)$$

Based on the immersion results and the surface characterization in Fig. 5, and Fig. 6, the HF-JDBM samples in α-MEM released Mg^{2+} consistently at a constant rate, and the total amount of Mg^{2+} was the highest among three coating groups after 28 days of immersion. The highly cracked surface morphology further revealed its limited protection against Mg substrate corrosion. In the EDS analysis, the generation of Ca, P, and O elements verified the deposition of CaP compounds during degradation. The short-term protection ability of MgF_2 was previously proved by the results of J Zhang and coworkers that MgF_2 lost its protection capability after 10 days, which thus impeded the clinical application of Mg alloys [31].

Thereby, a DCPD coating was designed to improve the corrosion resistance by impeding the water diffusion and ion assault and promote bioactivity at the same time [23]. The electrochemical test presented the improved corrosion resistance of DCPD coating. In the first 14 days of the immersion test, the Mg^{2+} released was suppressed by DCPD coating. However, the high solubility of the DCPD led to the deprotonation following the reaction (eq. 10 and eq. 11):

$$CaHPO_4{\cdot}2H_2O\ (s) \longrightarrow Ca^{2+} + HPO_4^{2-} + 2H_2O \qquad (10)$$

$$HPO_4^{2-} \leftrightarrow H^+ + PO_4^{3-} \qquad (11)$$

Consequently, it caused a gradual decrease in the pH from day 3 to day 10 and eventually reached the minimum value of ~7.4 on day 7. In the last 14 days, the corrosion rate of DCPD was accelerated even higher than that of HF-JDBM, evidenced by a dramatic elevation of Mg^{2+} release. Consequently, part of the coating was peeled off, with notable corrosion pits formed on the substrate surface. The ratio of Ca/P (1.46) was higher than that of DCPD, but closer to the stoichiometric Ca/P ratio of hydroxyapatite (1.67), indicating part of the DCPD coating converted to HA during 28 days immersion in the culture medium. As reported in previous works in our group, the Ca/P ratio of DCPD was measured about 1.33 after 21 days of immersion in m-SBF buffer solution, which might be due to the induction of HA precipitation after exposure to SBF[32].

In this study, hydrothermal conversion of DCPD coating with the dense structure was designed to generate HA coatings with unchanged compact topography in micro-scale to protect Mg alloys in long-term degradation. The performance of the HA coating with no internal crack/defect and increased thickness was attributable to the self-induced growth capacity of the coating in medium to well maintain the coating integrity as an effective barrier layer. In the electrochemical test, the tendency of pitting corrosion was obviously inhibited by hydrothermal treatment, clearly indicating the good stability and compactness of the obtained hydroxyapatite coating. Moreover, in the immersion test, HA with low degradation rate provides local alkaline microenvironment in body fluid, further contributing to a substantial enhancement of corrosion protection as compared to the DCPD, displaying a controlled, near-linear degradation profile of 0.036 mm/year, presenting great potential in orthopedic clinical applications. Surface HA induced nucleation and growth, leading to an increase of HA-12h thickness (eq. 12), further underlining its desirable properties of great stability and corrosion protection.

$10Ca^{2+} + 6PO_4^{3-} + 2OH^- \longrightarrow Ca_{10}(PO_4)_6(OH)_2$ (s) (12)

4.3 Cytocompatibility, activity and potential factors

In vitro biocompatibility evaluations of CaP-coated JDBM alloy were prerequisites for clinic applications by building up a systematical analysis. For the coated JDBM, the microenvironment of osteoblasts was affected by different factors such as the chemical composition, surface morphology, and degradation behavior of materials. These factors simultaneously exerted an essential impact on cell behaviors including cell adhesion, proliferation, and differentiation.

According to the cell proliferation results, MC3T3-E1 cells in the DCPD and HA-1h extracts exhibited a higher proliferation rate than those in control, while the HF-JDBM group expressed slightly lower cell activity than the control group during 3 days culture (Fig. 7a). This result could be correlated to the *in vitro* degradation tests, where the concentration of Mg^{2+}, pH value and osmolality in the extracts were considered as the predominant factors on cell viability. They were modulated to various extents based on the chemical property of the coating materials in 3-day immersion but controlled below 360 ppm of Mg^{2+} concentration, 7.4-7.8 of pH value and 300-500 mOsmol/kg of osmolality, which were critical doses without inhibiting MC3T3-E1 growth, as documented in previous work [33]. Furthermore, MC3T3-E1 cells displayed superior viability in the DCPD group. In the process of DCPD extract preparation, Mg degradation was significantly slowed down initially, and the concentration of Ca^{2+} rose because of the hydrolysis of DCPD (Fig. 4). It was previously reported that the increase of extracellular Ca^{2+} concentration was beneficial to cell survival and proliferation through the calcium-sensing receptor (CaR) [34]. The minimum Ca^{2+} concentration for maintaining cellular activity was about 1.8 mM, similar to that supplied in α-MEM, and lower Ca^{2+} concentration significantly prevented the cell growth

[35]. In consideration of this factor, the DCPD coating provided a more favorable microenvironment for cell proliferation in the early stage of cell culture.

The direct cell adhesion and proliferation assays are more complex than cell viability evaluations in extracts, due to the influences by various parameters, such as interfacial properties and local enrichment of degradation products, which may be responsible for the reduced cell activity of HF-JDBM. All of CaP coated groups demonstrated superior cytocompatibility of MC3T3-E1 cells on day 1, presumably due to their protection against Mg corrosion, and their similarity to the mineral component of bones. On day 3, poor cell proliferation was found on the HF-JDBM sample. For all of the hydrothermally treated samples, the number of cells significantly increased during 3 days culture, while it was slightly inferior to that of the DCPD and control group. This result might be correlated with the decrease of [Ca^{2+}] within three days of immersion, as mentioned above. It was found that lowering the [Ca^{2+}] to 20 ppm suppressed osteoblast proliferation in previous study [36, 37]. Details on cell-material interactions were further carefully analyzed with fluorescence staining and SEM. Cells on the DCPD and HA-1h exhibited elongated shape, with attachment to the edge of the grains. On the contrary, cells cultured on the HA-3h and HA-12h samples appeared well-spread shape, with a number of filopodia visible. Another important factor affecting cell adhesion would be the micro/nano topographical properties, which were demonstrated to regulate cell morphology and focal adhesion, facilitating cell-material attachment and improving biological performance [38]. It was previously reported that micro- and nano-structures synergistically affected the integrin activity, BMP-2 signaling pathway, and Cx43-related cell-cell communication [39]. This combination of interfacial structures in different scales is assumed to further enhance the biological activity of HA-coated JDBM.

HA, by itself, has been widely considered to facilitate osteoblastic differentiation and induce the bone regeneration process [40, 41]. In our study of HA coating on Mg, while the ALP activity of HF-JDBM and DCPD appeared lower than the control group, the distinctly elevated ALP activity in the HA-1h, HA-3h, and HA-12h groups suggested an enhanced osteogenic differentiation after 14 days of cell culture (Fig. 7c). Among all the three HA coating groups, the ALP level revealed the highest in the HA-1h, presumably due to the hydrolysis of OCP in the coating, which released inorganic phosphate (P_i) ions, similar as Sai et al. reported previously [42]. Additionally, we found the cells cultured in the HF-JDBM group had no differentiation capacity, which was most probably attributed to the over-high pH and released Mg^{2+} concentration [43]. Collectively, among the three different groups under investigation, HA-based coatings provide a most favorable interfacial environment for the Mg matrix to improve *in vitro* osteoinductivity properties, which was correlated with its chemical and morphological characteristics, and controlled degradation for Mg as well. A schematic illustration was proposed to summarize the coating formation, degradation process, and accordingly the effects on the cellular response (Fig. 8).

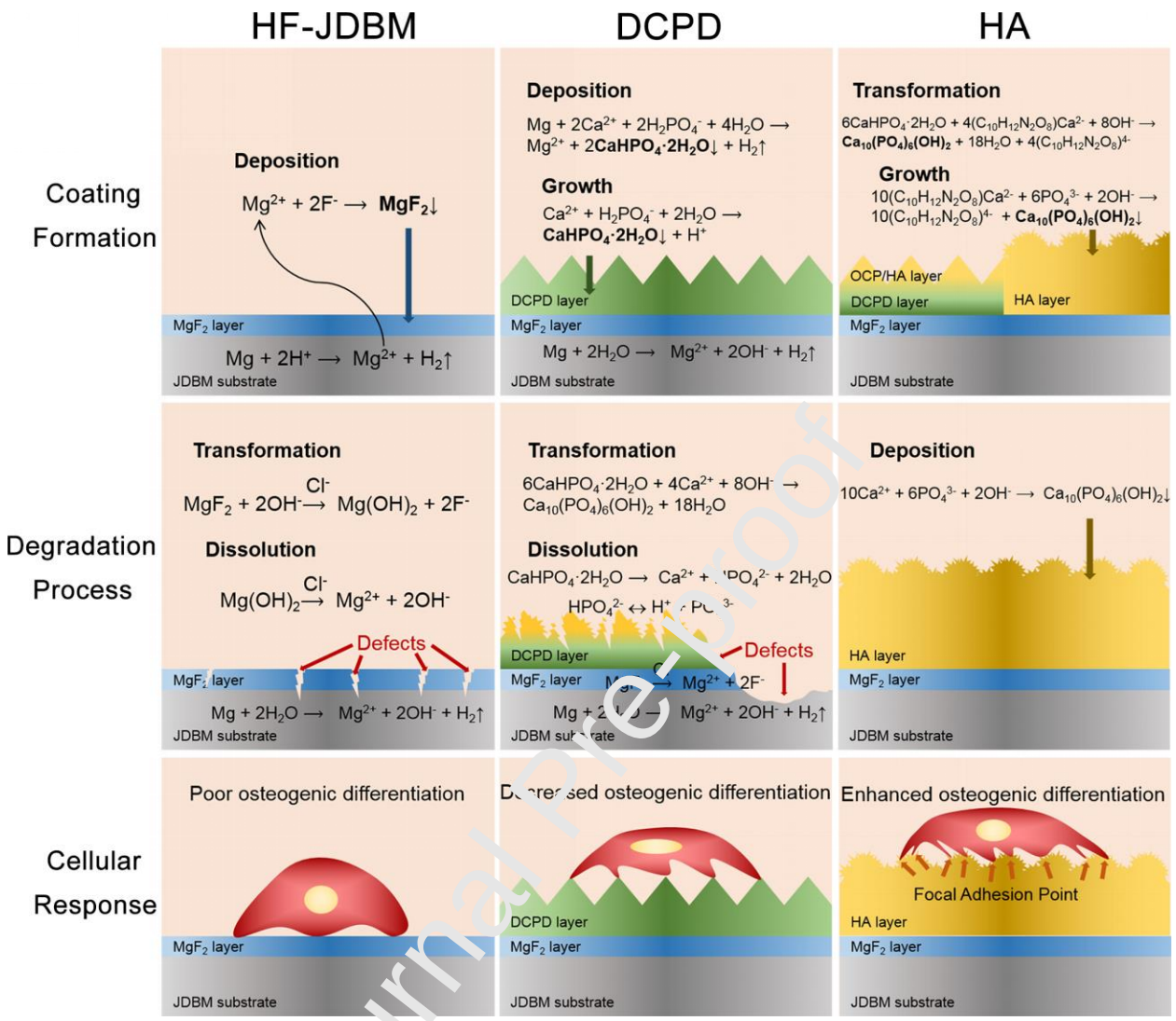

Figure 8. A schematic illustration of the coating formation, degradation process and cellular morphology of HF-JDBM, DCPD and HA samples.

5. Conclusions

The present work proposed convenient fabrication of HA-based coatings with controllable composition and structure on a biodegradable Mg-Nd-Zn-Zr alloy by low-temperature hydrothermal treatment of DCPD pre-coating. It demonstrated a continuous process of local dissolution and reprecipitation mechanism and *in-situ* conversion process of the coatings. The

HA coating of high pitting corrosion resistance and low corrosion rate in the long-term test, intrinsic weak alkalinity, low degradation rate, self-induced growth capacity, and obtained dense structure significantly enhanced the *in vitro* Mg corrosion resistance in comparison with MgF_2 and DCPD coatings. Moreover, a controllable degradation microenvironment and the hierarchical morphology of the coating revealed salutary effects on cytocompatibility and osteogenic differentiation *in vitro*. Collectively, compact HA coatings generated on JDBM alloys with hierarchical structure achieve both excellent corrosion resistance and favorable biocompatibility, showing great potential for a variety of temporary orthopedic implants applications.

Author Contributions

The manuscript was written through contributions of all authors. All authors have given approval to the final version of the manuscript.

Data availability

The raw/processed data required to reproduce these findings cannot be shared at this time as the data also forms part of an ongoing study.

Declaration of competing interest

The authors declare that they have no known competing financial interests or personal relationships that could have appeared to influence the work reported in this paper.

Acknowledgement

This work was financially supported by National Key Research and Development Program of

China (2016YFB0301001), Shanghai Municipal Commission of Economy and Information (JJ-YJCX-01-19-1277), Intelligent Manufacturing Project of Lin-gang Area in Shanghai City (ZN2018010212), the Science and Technology Commission of Shanghai Municipality (19441906300) and Shanghai Rising-Star Program (19QB1400400).

References

[1] D.W. Zhao, F. Witte, F.Q. Lu, J.L. Wang, J.L. Li, L. Qin, Current status on clinical applications of magnesium-based orthopaedic implants: A review from clinical translational perspective, Biomaterials, 112 (2017) 287-302. http://doi.org/10.1016/j.biomaterials.2016.10.017

[2] H. Hornberger, S. Virtanen, A.R. Boccaccini, Biomedical coatings on magnesium alloys - A review, Acta Biomater, 8 (2012) 2442-2455. http://doi.org/10.1016/j.actbio.2012.04.012

[3] F. Witte, V. Kaese, H. Haferkamp, E. Switzer, A. Meyer-Lindenberg, C.J. Wirth, H. Windhagen, In vivo corrosion of four magnesium alloys and the associated bone response, Biomaterials, 26 (2005) 3557-3563. http://doi.org/10.1016/j.biomaterials.2004.09.049

[4] X. Zhang, X.W. Li, J.G. Li, X.D. Sun, Preparation and Characterizations of Bioglass Ceramic Cement/Ca-P Coating on Pure Magnesium for Biomedical Applications, Acs Appl Mater Inter, 6 (2014) 513-525. http://doi.org/10.1021/am404574t

[5] L.M. Chang, L.F. Tian, W. Liu, X.Y. Duan, Formation of dicalcium phosphate dihydrate on magnesium alloy by micro-arc oxidation coupled with hydrothermal treatment, Corros Sci, 72 (2013) 118-124. http://doi.org/10.1016/j.corsci.2013.03.017

[6] X. Li, X.M. Liu, S.L. Wu, K.W.K. Yeung, Y.F. Zheng, P.K. Chu, Design of magnesium alloys with controllable degradation for biomedical implants: From bulk to surface, Acta Biomater, 45 (2016) 2-30. http://doi.org/10.1016/j.actbio.2016.09.005

[7] D.O. Costa, S.J. Dixon, A.S. Rizkalla, One- and Three-Dimensional Growth of Hydroxyapatite Nanowires during Sol-Gel-Hydrothermal Synthesis, Acs Appl Mater Inter, 4 (2012) 1490-1499. http://doi.org/10.1021/am201735k

[8] I.V. Fadeev, L.I. Shvorneva, S.M. Barinov, V.P. Orlovskii, Synthesis and structure of magnesium-substituted hydroxyapatite, Inorg Mater+, 39 (2003) 947-950. http://doi.org/Doi 10.1023/A:1025509305805

[9] R. Rojaee, M. Fathi, K. Raeissi, Controlling the degradation rate of AZ91 magnesium alloy via sol-gel derived nanostructured hydroxyapatite coating, Mat Sci Eng C-Mater, 33 (2013) 3817-3825. http://doi.org/10.1016/j.msec.2013.05.014

[10] H.R. Bakhsheshi-Rad, M.H. Idris, M.R. Abdul-Kadir, Synthesis and in vitro degradation evaluation of the nano-HA/MgF2 and DCPD/MgF2 composite coating on biodegradable Mg-Ca-Zn alloy, Surf Coat Tech, 222 (2013) 79-89. http://doi.org/10.1016/j.surfcoat.2013.02.007

[11] M. Tomozawa, S. Hiromoto, Microstructure of hydroxyapatite- and octacalcium phosphate-coatings formed on magnesium by a hydrothermal treatment at various pH values, Acta Mater, 59 (2011) 355-363. http://doi.org/10.1016/j.actamat.2010.09.041

[12] C.L. Wen, S.K. Guan, L. Peng, C.X. Ren, X. Wang, Z.H. Hu, Characterization and degradation behavior of AZ31 alloy surface modified by bone-like hydroxyapatite for implant applications, Appl Surf Sci, 255 (2009) 6433-6438. http://doi.org/10.1016/j.apsusc.2008.09.078

[13] M. Wang, J.Y. Gao, C. Shi, Y.C. Zhu, Y. Zeng, D.L. Wang, Facile One-Pot Synthesis of Oriented Pure Hydroxyapatite with Hierarchical Architecture by Topotactic Conversion, Cryst Growth Des, 14 (2014) 6459-6466. http://doi.org/10.1021/cg5013044

[14] D.N. da Rocha, M.H.P. da Silva, J.B. de Campos, R.L.S.B. Marcal, D.Q. Mijares, P.G. Coelho, L.R. Cruz, Kinetics of conversion of brushite coatings to hydroxyapatite in alkaline solution, J Mater Res Technol, 7 (2018) 479-486. http://doi.org/10.1016/j.jmrt.2018.02.002

[15] M. Kumar, H. Dasarathy, C. Riley, Electrodeposition of brushite coatings and their transformation to hydroxyapatite in aqueous solutions, J Biomed Mater Res, 45 (1999) 302-310. http://doi.org/Doi 10.1002/(Sici)1097-4636(19990615)45:4<302::Aid-Jbm4>3.0.Co;2-A

[16] C.T. Kwok, P.K. Wong, F.T. Cheng, H.C. Man, Characterization and corrosion behavior of hydroxyapatite coatings on Ti6Al4V fabricated by electrophoretic deposition, Appl Surf Sci, 255 (2009) 6736-6744. http://doi.org/10.1016/j.apsusc.2009.02.086

[17] Y.C. Su, L.Y. Niu, Y.B. Lu, J.S. Lian, G.Y. Li, Preparation and Corrosion Behavior of Calcium Phosphate and Hydroxyapatite Conversion Coatings on AM60 Magnesium Alloy, J Electrochem Soc, 160 (2013) C536-C541. http://doi.org/10.1149/2.036311jes

[18] A.F. Mavrogenis, R. Dimitriou, J. Parvizi, G.C. Babis, Biology of implant osseointegration, J Musculoskel Neuron, 9 (2009) 61-71.

[19] U.G.K. Wegst, H. Bai, E. Saiz, A.P. Tomsia, R.O. Ritchie, Bioinspired structural materials, Nat Mater, 14 (2015) 23-36. http://doi.org/10.1038/NMAT4089

[20] L.Z. Zhao, S.L. Mei, P.K. Chu, Y.M. Zhang, Z.F. Wu, The influence of hierarchical hybrid micro/nano-textured titanium surface with titania nanotubes on osteoblast functions, Biomaterials, 31 (2010) 5072-5082. http://doi.org/10.1016/j.biomaterials.2010.03.014

[21] J. Tan, W.M. Saltzman, Biomaterials with hierarchically defined micro- and nanoscale structure, Biomaterials, 25 (2004) 3593-3601. http://doi.org/10.1016/j.biomaterials.2003.10.034

[22] X.B. Zhang, G.Y. Yuan, L. Mao, J.L. Niu, P.H. Fu, W.J. Ding, Effects of extrusion and heat treatment on the mechanical properties and biocorrosion behaviors of a Mg-Nd-Zn-Zr alloy, J Mech Behav Biomed, 7 (2012) 77-86. http://doi.org/10.1016/j.jmbbm.2011.05.026

[23] J.L. Niu, G.Y. Yuan, Y. Liao, L. Mao, J. Zhang, Y.P. Wang, F. Huang, Y. Jiang, Y.H. He, W.J. Ding, Enhanced biocorrosion resistance and biocompatibility of degradable Mg-Nd-Zn-Zr alloy by brushite coating, Mat Sci Eng C-Mater, 33 (2013) 4833-4841. http://doi.org/10.1016/j.msec.2013.08.008

[24] C. Cardell, I. Guerra, An overview of emerging hyphenated SEM-EDX and Raman spectroscopy systems:

Applications in life, environmental and materials sciences, Trac-Trend Anal Chem, 77 (2016) 156-166. http://doi.org/10.1016/j.trac.2015.12.001

[25] S. Mandel, A.C. Tas, Brushite (CaHPO4 center dot 2H(2)O) to octacalcium phosphate (Ca-8(HPO4)(2)(PO4)(4)center dot 5H(2)O) transformation in DMEM solutions at 36.5 degrees C, Mat Sci Eng C-Mater, 30 (2010) 245-254. http://doi.org/10.1016/j.msec.2009.10.009

[26] N. Ohtsu, S. Hiromoto, M. Yamane, K. Satoh, M. Tomozawa, Chemical and crystallographic characterizations of hydroxyapatite- and octacalcium phosphate-coatings on magnesium synthesized by chemical solution deposition using XPS and XRD, Surf Coat Tech, 218 (2013) 114-118. http://doi.org/10.1016/j.surfcoat.2012.12.037

[27] M. Tomozawa, S. Hiromoto, Y. Harada, Microstructure of hydroxyapatite-coated magnesium prepared in aqueous solution, Surf Coat Tech, 204 (2010) 3243-3247. http://doi.org/10.1016/j.surfcoat.2010.03.023

[28] Y.C. Qi, J. Shen, Q.Y. Jiang, B. Jin, J.W. Chen, X. Zhang, The morphology control of hydroxyapatite microsphere at high pH values by hydrothermal method, Adv Powder Technol, 26 (2015) 1041-1046. http://doi.org/10.1016/j.apt.2015.04.008

[29] L. Mao, L. Shen, J.H. Chen, Y. Wu, M. Kwak, Y. Lu, Q. Xue, J. Pei, L. Zhang, G.Y. Yuan, R. Fan, J.B. Ge, W.J. Ding, Enhanced Bioactivity of Mg-Nd-Zn-Zr Alloy Achieved with Nanoscale MgF2 Surface for Vascular Stent Application, Acs Appl Mater Inter, 7 (2015) 5320-5330. http://doi.org/10.1021/am5086885

[30] Y.J. Shi, J. Pei, J. Zhang, J.L. Niu, H. Zhang, S.R. Guo, Z.H. Li, G.Y. Yuan, Enhanced corrosion resistance and cytocompatibility of biodegradable Mg alloys by introduction of Mg(OH)(2) particles into poly (L-lactic acid) coating, Sci Rep-Uk, 7 (2017). http://doi.org/ARTN 41796

10.1038/srep41796

[31] J. Zhang, N. Kong, J.L. Niu, Y.J. Shi, H.Y. Li, Y. Zhou, G.Y. Yuan, Influence of fluoride treatment on surface properties, biodegradation and cytocompatibility of Mg-Nd-Zn-Zr alloy, J Mater Sci-Mater M, 25 (2014) 791-799. http://doi.org/10.1007/s10856-013-5106-z

[32] L. Zhang, J. Pei, H.D. Wang, Y.J. Shi, J.L. Niu, F. Yuan, H. Huang, H. Zhang, G.Y. Yuan, Facile Preparation of Poly(lactic acid)/Brushite Bilayer Coating on Biodegradable Magnesium Alloys with Multiple Functionalities for Orthopedic Application, Acs Appl Mater Inter, 9 (2017) 9437-9448. http://doi.org/10.1021/acsami.7b00209

[33] J.L. Wang, F. Witte, T.F. Xi, Y.F. Zheng, K. Yang, Y.S. Yang, D.W. Zhao, J. Meng, Y.D. Li, W.R. Li, K.M. Chan, L. Qin, Recommendation for modifying current cytotoxicity testing standards for biodegradable magnesium-based materials, Acta Biomater, 21 (2015) 237-249. http://doi.org/10.1016/j.actbio.2015.04.011

[34] M.M. Dvorak, A. Siddiqua, D.T. Ward, D.H. Carter, S.L. Dallas, E.F. Nemeth, D. Riccardi, Physiological changes in extracellular calcium concentration directly control osteoblast function in the absence of calciotropic hormones, P Natl Acad Sci USA, 101 (2004) 5140-5145. http://doi.org/10.1073/pnas.0306141101

[35] Y.K. Liu, Q.Z. Lu, R. Pei, H.J. Ji, G.S. Zhou, X.L. Zhao, R.K. Tang, M. Zhang, The effect of extracellular calcium and inorganic phosphate on the growth and osteogenic differentiation of mesenchymal stem cells in vitro: implication for bone tissue engineering, Biomed Mater, 4 (2009). http://doi.org/Artn 025004

10.1088/1748-6041/4/2/025004

[36] Z. Meleti, I.M. Shapiro, C.S. Adams, Inorganic phosphate induces apoptosis of osteoblast-like cells in culture, Bone, 27 (2000) 359-366. http://doi.org/10.1016/S8756-3282(00)00346-X

[37] J.M. Sadowska, J. Guillem-Marti, E.B. Montufar, M. Espanol, M.P. Ginebra, Biomimetic Versus Sintered Calcium Phosphates: The In Vitro Behavior of Osteoblasts and Mesenchymal Stem Cells, Tissue Eng Pt A, 23 (2017) 1297-1309. http://doi.org/10.1089/ten.tea.2016.0406

[38] A. Martins, S. Chung, A.J. Pedro, R.A. Sousa, A.P. Marques, R.L. Reis, N.M. Neves, Hierarchical starch-based fibrous scaffold for bone tissue engineering applications, J Tissue Eng Regen M, 3 (2009) 37-42. http://doi.org/10.1002/term.132

[39] C.C. Zhao, X.Y. Wang, L. Gao, L.G. Jing, Q. Zhou, J. Chang, The role of the micro-pattern and nano-topography of hydroxyapatite bioceramics on stimulating osteogenic differentiation of mesenchymal stem cells, Acta Biomater, 73 (2018) 509-+. http://doi.org/10.1016/j.actbio.2018.04.030

[40] R. Shu, R. McMullen, M.J. Baumann, L.R. McCabe, Hydroxyapatite accelerates differentiation and suppresses growth of MC3T3-E1 osteoblasts, J Biomed Mater Res A, 67a (2003) 1196-1204. http://doi.org/10.1002/jbm.a.20021

[41] R.A. Surmenev, M.A. Surmeneva, A.A. Ivanova, Significance of calcium phosphate coatings for the enhancement of new bone osteogenesis - A review, Acta Biomater, 10 (2014) 557-579. http://doi.org/10.1016/j.actbio.2013.10.036

[42] Y. Sai, Y. Shiwaku, T. Anada, K. Tsuchiya, T. Takahashi, O. Suzuki, Capacity of octacalcium phosphate to promote osteoblastic differentiation toward osteocytes in vitro, Acta Biomater, 69 (2018) 362-371. http://doi.org/10.1016/j.actbio.2018.01.026

[43] M. Leidi, F. Dellera, M. Mariotti, J.A.M. Maier, High magnesium inhibits human osteoblast differentiation in vitro, Magnesium Res, 24 (2011) 1-6. http://doi.org/10.1684/mrh.2011.0271

Contribution statement

Mingyu You: Concetualization, Methodology, Writing - original draft, Writing - review & editing. **Mónica Echeverry-Rendón:** Conceptualization, Methodology, Writing - review & editing. **Lei Zhang:** Methodology. **Jialin Niu:** Methodology. **Jian Zhang:** Investigation. **Jia Pei:** Conceptualization, Writing - review & editing, Supervision, Funding acquisition. **Guangyin Yuan:** Conceptualization, Writing - review & editing, Supervision, Funding acquisition.

Declaration of interests

☒ The authors declare that they have no known competing financial interests or personal relationships that could have appeared to influence the work reported in this paper.

☐The authors declare the following financial interests/personal relationships which may be considered as potential competing interests:

Highlights

1. Hierarchically structured HA coatings are developed on Mg by hydrothermal conversion.

2. Local dissolution and reprecipitation mechanism from brushite precursor are elucidated.

3. The HA coating greatly impedes Mg corrosion owing to its compact structure and alkalinity.

4. The HA coating provides favorable microenvironment to improve *in vitro* osteoinductivity.